PNAS RESEARCH ARTICLE | APPLIED PHYSICAL SCIENCES

Asymmetric fluctuations and self-folding of active interfaces

Liang Zhao[a,1], Paarth Gulati[a,1], Fernando Caballero[a,b], Itamar Kolvin[a,c], Raymond Adkins[a,d], M. Cristina Marchetti[a,e,2], and Zvonimir Dogic[a,e,2]

Affiliations are included on p. 9.

Edited by Michael Cates, University of Cambridge, Cambridge, United Kingdom; received May 25, 2024; accepted October 24, 2024

We study the structure and dynamics of the interface separating a passive fluid from a microtubule-based active fluid. Turbulent-like active flows power giant interfacial fluctuations, which exhibit pronounced asymmetry between regions of positive and negative curvature. Experiments, numerical simulations, and theoretical arguments reveal how the interface breaks up the spatial symmetry of the fundamental bend instability to generate local vortical flows that lead to asymmetric interface fluctuations. The magnitude of interface deformations increases with activity: In the high activity limit, the interface self-folds invaginating passive droplets and generating a foam-like phase, where active fluid is perforated with passive droplets. These results demonstrate how active stresses control the structure, dynamics, and break-up of soft, deformable, and reconfigurable liquid–liquid interfaces.

active fluid | liquid–liquid phase separation | interfaces

Significance

Liquid–liquid phase separation is ubiquitous throughout biology, physics, materials science, and everyday life. Controlling interfaces is essential for forming organelles in cells and developing new materials. Traditional control of fluid interfaces relies on chemistry and interface-modifying agents such as surfactants and detergents. By merging a binary phase separating polymer solution with a microtubule-based active fluid, we demonstrate that activity provides a handle for interface control. Spontaneous flows generated through the active phase drive giant interfacial fluctuations and ultimately their disintegration. Our results reveal a mechanical mechanism for tuning interfaces and droplets, generating conformations and morphologies inaccessible to conventional chemistry-based equilibrium techniques.

Bulk active fluids composed of extensile rods are inherently unstable (1). An initially uniformly aligned state rapidly evolves into steady-state turbulent-like dynamics through the amplification of infinitesimal bend distortions by the active stresses (2–14). Active fluids exhibit a complex interplay with rigid boundaries, geometrical confinements, and deformable interfaces or membranes. On the one hand, rigid and immutable boundaries dramatically change the structure and dynamics of a bulk-active fluid. For example, geometrical confinement transforms bulk chaotic dynamics into coherent long-ranged flows capable of efficient mass transport (15–23). On the other hand, the active fluid can exert stresses on soft and deformable interfaces and membranes, regulating their structure and dynamics and generating conformations and morphologies that are not accessible in equilibrium. For example, in biological cells, a deformable lipid membrane interacts with the stress-generating actin cortex to enable essential processes, such as blebbing, endo and exo-cytosis, cell division, and wound-healing (24–27). It is, however, challenging to elucidate universal physical principles in complex biological cells. Progress can instead be made by studying simplified systems (28–41).

So far, experiments have mostly explored active fluids confined within finite-sized lipid vesicles or droplets (42–48). We study microtubule-based active fluids that exhibit long-ranged turbulent-like flows and can be prepared in milliliter quantities (2). Using a recently developed system (35), we explore how such bulk fluids interact with macroscale deformable and reconfigurable interfaces that are created by liquid–liquid phase separation. The active fluid partitions into one of the two phases, generating active stresses that power dramatic interfacial fluctuations. Active interfaces exhibit a pronounced up–down asymmetry in the local curvature, which is explained by how the interface breaks the spatial symmetry of the ubiquitous bend instability. Increasing the activity beyond a critical value leads to giant fluctuations where the interface folds on itself, enveloping passive droplets and generating foam-like perforated phases.

Experimental Realization of a Bulk Active Interface

The passive phase-separating system was a mixture of polyethylene glycol (PEG, 100 kDa) and dextran (500 kDa) dissolved in an aqueous buffer. At high polymer concentration, this mixture separated into a PEG-rich and a dextran-rich phase (49). We merged the PEG/dextran mixture with an active fluid, which contained MTs and force-generating kinesin-streptavidin clusters (KSA) (35). The active fluid components strongly partitioned into the dextran phase where microtubules (MTs) bundled due to the depletion attraction (Fig. 1*D*) (50). The KSA clusters crosslinked multiple MTs within a bundle. The ATP (Adenosine triphosphate)-fueled stepping of kinesin motors drove interfilament sliding, which generated extensile active stresses that powered

Author contributions: L.Z., M.C.M., and Z.D. designed research; L.Z., P.G., F.C., and R.A. performed research; L.Z., P.G., F.C., and I.K. analyzed data; I.K. and R.A. developed the experimental system; R.A. developed the imaging method; and L.Z., P.G., M.C.M., and Z.D. wrote the paper.

The authors declare no competing interest.

This article is a PNAS Direct Submission.

[1]L.Z. and P.G. contributed equally to this work.

[2]To whom correspondence may be addressed. Email: mcmarche@ucsb.edu or zdogic@ucsb.edu.

This article contains supporting information online at https://www.pnas.org/lookup/suppl/doi:10.1073/pnas.2410345121/-/DCSupplemental.

Published December 10, 2024.

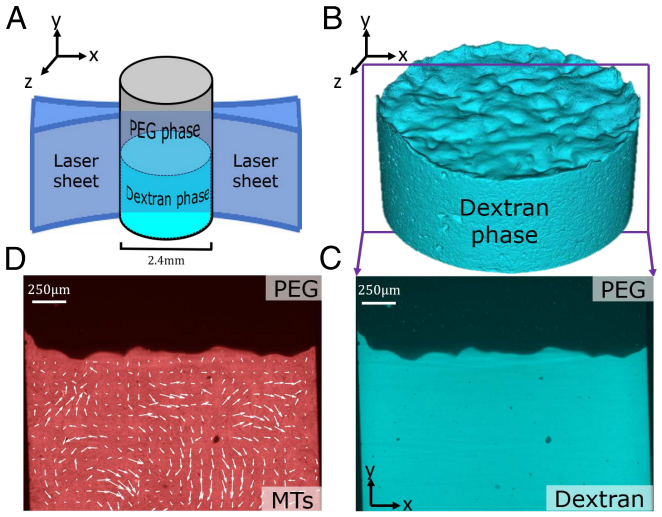

Fig. 1. Bulk phase separation between an active and a passive phase. (*A*) Experimental setup used for imaging the active interface. The sample was loaded into a transparent cylindrical tube, where it separated into a passive *Top* PEG-rich layer and a *Bottom* dextran-rich layer (cyan) that contained the MT-based active fluid. The sample was illuminated with a laser sheet. The $x-y$ plane was imaged by an objective aligned along the z direction. The tube's inner diameter was 2.4 mm. (*B*) Fluorescent dextran phase, reconstructed from 2D $x-y$ images at 120 different z positions. (*C*) A vertical $x-y$ slice in the *Middle* of the cylinder. Dextran is indicated in cyan. (*D*) The same slice was imaged in the MT (red) channel. MTs strongly partition with the dextran phase. White arrows are the 2D velocity field. The sample contained 129 nM KSA, 2.1% PEG, and 2.1% dextran.

turbulent-like dynamics throughout the dextran phase. The MT volume fraction was only 0.1%. Therefore, in the absence of activity, they form isotropic liquid crystals. Activity-induced local nematic order (*SI Appendix*, Fig. S11) (51, 52). An ATP-regeneration system sustained the active dynamics for several hours.

Previous studies explored MT-based active fluids next to an oil–water interface, which did not exhibit visible fluctuations due to a large surface tension (2). Here, we used PEG/dextran mixtures which lowered interfacial tension by several orders of magnitude (49). We optimized PEG/dextran concentrations and molecular weights to simultaneously exhibit interfacial fluctuations and drive efficient MT bundling essential for generation of active stress. We studied a "high" interfacial tension mixture of 2.1% PEG and 2.1% dextran, and a "low" interfacial tension mixture of 2.0% PEG and 2.0% dextran (*SI Appendix*, Fig. S12).

Active interfaces and associated phase separation were previously studied in a quasi-2D confinement (35). In this regime, the strong frictional interaction with the confining walls suppressed the interface mobility and limited the magnitude and range of active flows. Additionally, the interface exhibited activity-induced wetting, which spread the active phase along the confining walls and changed the interface structure. To minimize boundary effects and frictional interactions, we created a 2D active interface that separated a bulk 3D active fluid and a 3D passive fluid. The active mixture was placed in a cylindrical chamber, where it phase-separated into PEG-rich and dextran-rich components. Brief centrifugation generated bulk phase separation (Fig. 1*A*). A fraction of the dextran and the MTs were fluorescently tagged. Samples were imaged with a light sheet microscope (Zeiss Z.1 Lightsheet). Volumes were reconstructed from $x-y$ cross-sections obtained at successive z positions with a step size of 20 μm (Fig. 1*B*). Scanning a 200 μm thick section in two channels required 3.5 s and scanning a 600 μm section in one channel required 4.3 s.

Immediately after centrifuging, the interface was flat. Spontaneous flows developed in the active phase generated interfacial deformations on the scale of 10's of microns (Fig. 1 *B–D*) (35). The amplitude of interfacial fluctuations, which is a proxy to the active forces operating at the interface, increased with time (*SI Appendix*, Figs. S13 and S14 and Movie S1). The magnitude of interfacial fluctuations was correlated with the KSA concentration in the range of 45 nM to 180 nM (Fig. 2 and Movie S2).

Continuum Model of Active Phase Separation

To gain a qualitative understanding of the experimental findings, we explored a continuum model of active interfaces (30, 35, 47, 53). The model was implemented in two dimensions, with a one-dimensional interface separating the active and passive phases. In contrast to previous work (35), we ignore frictional dissipation which is not relevant for the bulk geometry of the experiments. Despite different dimensionality, both simulations and experiments allow for long-ranged active flows that play an important role in driving the anisotropy of interfacial fluctuations. The hydrodynamic equations were numerically solved for a mixture of an active liquid crystal and a passive fluid, given by

$$\begin{aligned} D_t\phi &= M\nabla^2\mu, \\ D_t\mathbf{Q} &= \lambda\mathbf{A} - \boldsymbol{\omega}\cdot\mathbf{Q} + \mathbf{Q}\cdot\boldsymbol{\omega} + \frac{1}{\Gamma}\mathbf{H}, \\ 0 &= \eta\nabla^2\mathbf{v} - \nabla P + \nabla\cdot\boldsymbol{\sigma} + \mathbf{f}^g, \end{aligned} \qquad [1]$$

where ϕ is the concentration of active fluid, the nematic tensor $\mathbf{Q}$ describes the local orientational order in the active liquid crystal, and $\mathbf{v}$ is the flow velocity which advects both ϕ and $\mathbf{Q}$ through the material derivative $D_t = \partial_t + \mathbf{v}\cdot\nabla$. Phase separation between the active ($\phi = 1$) and passive ($\phi = 0$) phases is driven by the chemical potential $\mu = \delta F_\phi/\delta\phi$, where F_ϕ is the Cahn–Hilliard free energy, $F_\phi = (4\gamma/\xi)\int d\mathbf{r}\left(\phi^2(\phi-1)^2 + (\xi^2/2)(\nabla\phi)^2\right)$. Here, γ is the surface tension of the phase-separated mixture and ξ is the interface width.

The nematic order parameter $\mathbf{Q}$ is rotated by flow gradients quantified by the strain rate $A_{ij} = (\partial_i v_j + \partial_j v_i)/2$ and vorticity $\omega_{ij} = (\partial_i v_j - \partial_j v_i)/2$ and relaxes through $\mathbf{H} = -\delta F_Q/\delta\mathbf{Q}$, where F_Q is the Landau–de Gennes free energy for the mixture, $F_Q = \int d\mathbf{r}(r\phi/2)\mathrm{Tr}\mathbf{Q}^2 + (u/4)(\mathrm{Tr}\mathbf{Q}^2)^2 + (K/2)(\nabla\mathbf{Q})^2$, with Γ a rotational viscosity. Here, K is the nematic elastic modulus and $u > 0$. To model the experimental system, we choose $r > 0$, which ensures that in the absence of activity, the liquid crystal is in the isotropic phase.

The flow is governed by Stokes' equation and assumed incompressible, $\nabla\cdot\mathbf{v} = 0$. It is controlled by the interplay of viscous dissipation with viscosity η, pressure gradients, and passive and active stresses, $\boldsymbol{\sigma} = \boldsymbol{\sigma}^p + \boldsymbol{\sigma}^a$. The active stress $\boldsymbol{\sigma}^a = \alpha\phi\mathbf{Q}$ is controlled by the fraction ϕ of active fluid. The extensile nature of the liquid crystal is described by the activity $\alpha < 0$. Finally, $\mathbf{f}_g = -\hat{y}(\rho_0 + \phi\Delta\rho)g$ is the force due to gravity, with $\Delta\rho$ the difference in the densities of the two fluid phases. More details about the model are given in *SI Appendix*.

Active flows generate local nematic order through flow alignment (17, 51, 52). Above a critical activity $\alpha_0 = 2\eta r/\lambda\Gamma$, bulk isotropic active liquid crystals are linearly unstable and develop spatiotemporal chaotic flows similar to those observed in the nematic phase (31). We consider activities with magnitudes larger than α_0. We vary the surface tension γ, keeping the interface width fixed. We measure lengths in units of the interface

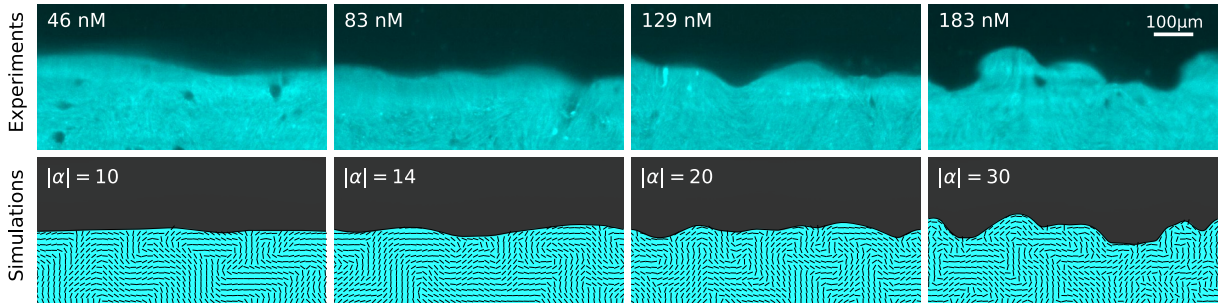

Fig. 2. Asymmetric interfacial fluctuations in experiments and simulations. *Top* row (Experiments): Two-dimensional cross-sections of the interface at increasing KSA concentrations. The amplitude of fluctuations increases with increasing KSA concentration. All samples contained 2.1% PEG and 2.1% dextran. The images were taken at $t = 2$ h. *Bottom* row (Simulations): Both the amplitude and asymmetry of the interfacial fluctuations increase with activity at a fixed surface tension, $\gamma = 500$. The passive and active phases are shown in black and cyan, respectively. The nematic director inside the active phase is plotted every 30 lattice sites. Only a portion of both experimental and simulation systems close to the bulk interface is shown here.

width ξ, times in units of the nematic reorientation time Γ/r, and stresses in units of liquid crystal energy density r. In these units, the other parameters in the model are fixed as follows: $u = 10.0, M = 0.67, K = 106.67, \eta = 1.0, \lambda = 1.0$, and $\Delta\rho g = 0.12$, which correspond to $\alpha_0 = 2.0$. We solve Eq. **1** numerically using self-developed pseudospectral solvers. All simulation results are shown for a regular grid with 1024×1024 lattice sites, and a total of $10^6 - 10^7$ time steps. Details about the numerical simulations are in *Materials and Methods* and *SI Appendix*.

Asymmetry of Fluctuating Active Interfaces

We first studied the "high"-surface-tension regime, where interfaces retained their integrity throughout most of the experiment. Careful inspection revealed a peculiar feature of such interfaces. Typical interfacial configurations, especially at higher activity, were characterized by steep and deep valleys wherein the passive phase protruded into the active phase (Fig. 2*A*). In contrast, the peaks of the active phase into the passive phase were shallow and smooth. Motivated by these observations, we calculated the local mean interface curvatures κ and plotted their distribution over the whole interface (Fig. 3*A*) (*Materials and Methods*). Positive curvatures indicated valleys where the passive phase protrudes into the active dextran phase (Fig. 3 *A*, *Inset*). The width of the distribution increased with increasing KSA concentrations, which controls sample activity (Fig. 3*A*). Additionally, the probability density of local curvature exhibited a pronounced asymmetry. For large amplitudes, the probability of observing positive curvatures was larger than the negative ones ($\rho(|\kappa|) > \rho(-|\kappa|)$). Since the distribution was measured along a plane, its average must be zero. Therefore, the asymmetric curvature distributions did not peak at $\kappa = 0$, but at a small negative value of κ. This quantification confirmed that the protrusions of the passive phase into the active phase were sharper and more pronounced than the reverse.

The interface reconfigures on a time scale of tens of seconds. Thus, over tens of minutes, it undergoes a sufficient number of independent conformations to allow for accurate measurement of the curvature distribution. Plotting the time evolution of such distributions over the sample lifetime reveals that the interface exhibited an intriguing aging effect (Fig. 3*B* and *SI Appendix*, Figs. S13 and S14 and Movie S1). The magnitude of the fluctuations and the width of the curvature distributions increased over time. This trend was similar for interfaces measured at a fixed time but with an increasing KSA concentration (Movie S2). It was also reported in the previous study of quasi-2D interfaces (35). These observations suggest that in MT-based active fluids, the active stress increases with time. The origin of this behavior is unknown.

To understand the asymmetry mechanism, we examined the behavior of the interface in the continuum model. The interface is defined as the locus of points corresponding to where the polymer concentration $\phi = 1/2$. We calculated the local curvature $\kappa(s)$ at the arclength s along the interface after the numerically integrated equations reached a steady state (*SI Appendix*, Fig. S5). The probability distribution of $\kappa(s)$ is asymmetric (Fig. 3*C*), as found

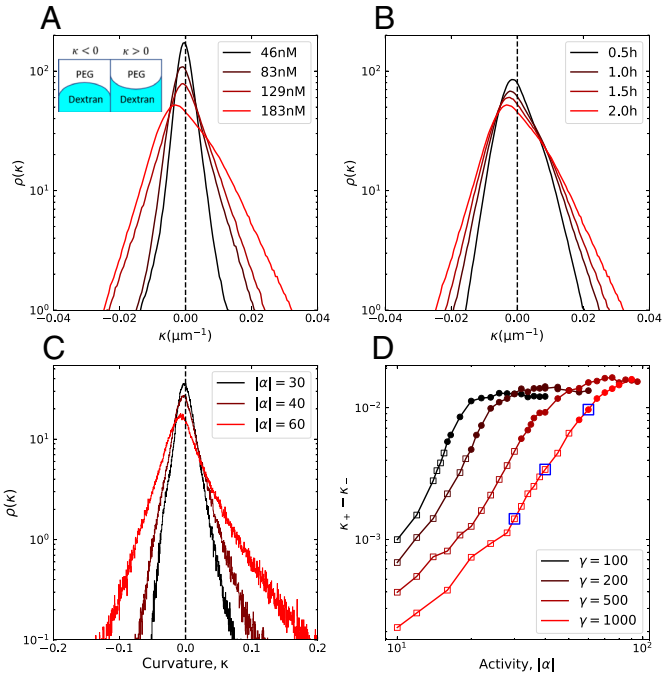

Fig. 3. Asymmetry in the probability distribution of local interface curvatures $\rho(\kappa)$. *Top* row (Experiments): (*A*) Curvature probability distribution $\rho(\kappa)$ for four KSA concentrations at time $t = 2$ h. *Inset*: defining κ sign. (*B*) Time evolution of $\rho(\kappa)$ for 183 nM KSA sample. Each curve is averaged over 30 min. All samples contain 2.1% PEG and 2.1% dextran. *Bottom* row (Simulations): (*C*) Curvature probability distribution at three values of activity α and fixed surface tension $\gamma = 1{,}000$. (*D*) The curvature asymmetry $\kappa_+ - \kappa_-$ (Eq. **2**) increases with increasing activity and with decreasing surface tension γ. The asymmetry saturates at large activity, where the interface breaks up due to the invagination of droplets of passive fluid into the active phase. Open and closed symbols correspond to states without and with droplet invagination. The blue squares correspond to the curvature distributions in panel *C*.

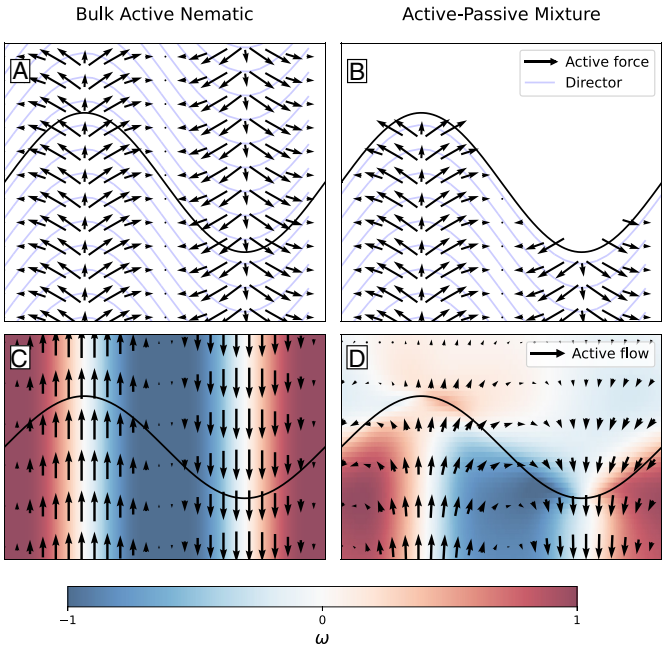

Fig. 4. Active forces and flows in a bulk active fluid and in a phase-separated mixture. (*A*) Analytically calculated active forces from a sinusoidal deformation of the director field in a bulk active fluid (*SI Appndix*, Eq. **S15**). Black arrows are active forces and light blue lines are the director field. The black solid line is a guide to the eye as there is no interface here. (*B*) Active forces from director deformations in a phase-separated active/passive mixture (*SI Appndix*, Eq. **S14**). The black solid line denotes the interface between passive (*Top*) and active (*Bottom*) fluids. (*C*) Active flows are obtained from the numerical solution of the Stokes equation for a bulk active fluid with the nematic configuration in the panel *Above*. The color map is vorticity ω. (*D*) In the phase-separated mixture, active forces are absent from the passive phase, leading to asymmetric tangential flows that deepen the valleys and broaden the peaks.

in experiments, with longer tails for $\kappa > 0$ than for $\kappa < 0$, corresponding to smooth peaks and deep valleys. The asymmetry is quantified by the difference between mean positive and negative curvatures, defined as

$$\kappa_+ = \frac{\int_0^\infty d\kappa\ \kappa\ \rho(\kappa)}{\int_0^\infty d\kappa\ \rho(\kappa)}; \quad \kappa_- = \left| \frac{\int_{-\infty}^0 d\kappa\ \kappa\ \rho(\kappa)}{\int_{-\infty}^0 d\kappa\ \rho(\kappa)} \right| . \qquad [2]$$

For symmetric fluctuations, $\kappa_+ - \kappa_- = 0$. We find that this difference increases with activity, but saturates at high activity (Fig. 3*D*).

We hypothesize that the asymmetry arises from the interplay between the interface-induced structures of the active fluid and the flows they generate. In aligned nematics, extensile activity creates effective interaction that aligns the director field with interfaces or walls (30, 54). We find that the same phenomenon, known as active anchoring, occurs in the isotropic active phase of extensile active liquid crystals (*SI Appendix*, Fig. S3). The thickness of the aligned layer is controlled by the active length scale $\ell_\alpha \sim \sqrt{K/|\alpha|}$ (*SI Appendix*, Fig. S4). Given the presence of a surface-induced aligned layer, we compare active forces and associated flows in a phase-separated active/passive mixture to those in a bulk active fluid. We analytically calculate the active forces induced by director deformations (Fig. 4 *A* and *B*) and the associated active flows obtained from the Stokes equation (Fig. 4 *C* and *D* and *SI Appendix*, section 2A). In a bulk active fluid, active forces yield the familiar bend instability which symmetrically enhances any director bend deformation (1). In the active/passive mixture, the force-generating active liquid crystal is located on only one side of the interface; active forces are absent in the passive phase. This creates an asymmetry in the flows that deepens and narrows the valleys into the active fluids while stretching and broadening out the shallow peaks (Fig. 4*D*). The asymmetry, due to the preferred alignment of the director with the interface, is exaggerated in this idealized limit with perfect anchoring. Similar vortical flows, however, arise due to active anchoring and give rise to curvature asymmetry.

This dynamical asymmetry becomes more evident by examining the evolution of a sinusoidal perturbation of the interface between a passive fluid and an active nematic with explicit director anchoring (Fig. 5). In this minimal model, the flow is driven by active forces and relaxes through the passive molecular field **H**, but does not directly rotate the nematic director (*SI Appendix*, section 3B). As the system evolves, the nematic texture reorients to remain parallel to the interface. In a mixture of two identical active nematics, the interface remains symmetric while evolving in time (Fig. 5 *A* and *C*). In contrast, in the active/passive mixture (Fig. 5 *B* and *D*), the flow deforms the interface asymmetrically, with sharp dips into the active phase. We note that the asymmetry is a nonlinear effect, driven by flows tangent to the interface. It cannot be recovered by linear stability analysis of a flat or uniformly curved interface that only includes normal active forces (38).

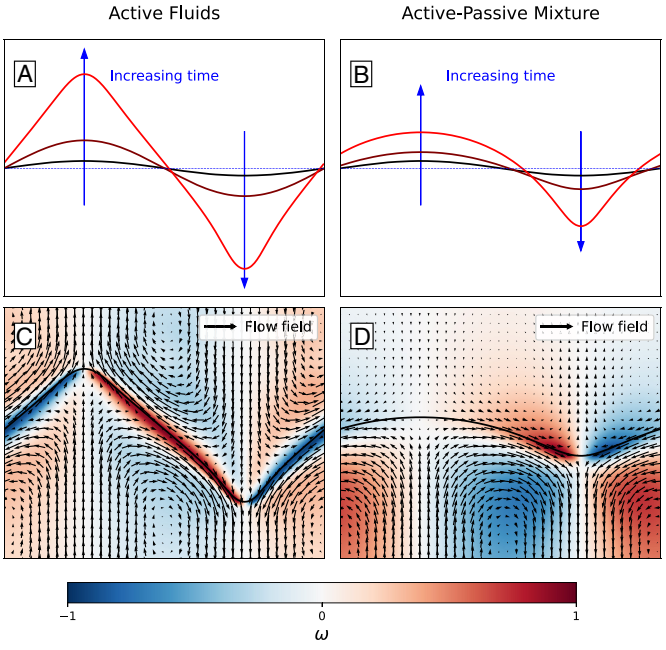

Fig. 5. Time evolution of an interface perturbation. The nematic is anchored to the interface, and flows are driven by active and interfacial stresses (*SI Appendix*, section 3B). (*A*) Time evolution (black to red) of a symmetric interface perturbation in the case of two identical active fluids *Above* and *Below* the interface. The time-evolving interface preserves the initial symmetry (*B*) Time evolution (black to red) of a symmetric interface perturbation in the case of an active fluid below the interface and a passive isotropic fluid *Above*. The initial symmetric perturbation of the interface builds curvature asymmetry i.e. it develops a deep valley and a broad peak. (*C*) Flow field near the interface in the case of identical active fluids for the interface configuration shown in red *Above*. Arrows depict the flow velocity and color indicates normalized vorticity ω. (*D*) Flows near the interface separate the active (*Below* the interface) and passive fluid (*Above* the interface) for the interface configuration shown in red *Above*. The interface experiences asymmetric vortical flows, resulting in curvature asymmetry.

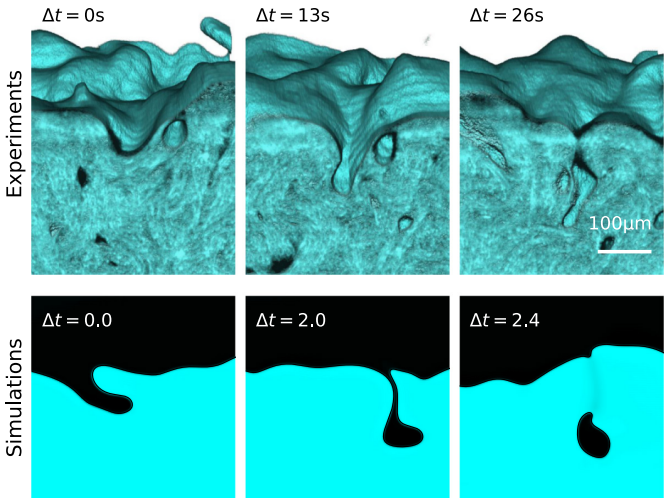

Fig. 6. Pathways of passive droplet invagination. *Top* row (Experiments): Invagination of a passive droplet by the active phase. The valley in the interface grows deeper with time. Eventually, the vertical walls merge to form a passive droplet enveloped by the active fluid (Movie S3). The red arrows mark the position of the invagination. *Bottom* row (Simulations): Invagination of a passive droplet into the active fluid observed in simulations ($\alpha = -20, \gamma = 200$, Movie S8 B).

Here we focused on experimentally relevant extensile active liquid crystals. The same asymmetry arises, however, in contractile flow tumbling fluids ($\alpha > 0, \lambda < 0$). In this case active anchoring preferentially aligns the director normal to the interface, but active flows are also rotated, resulting in the same behavior as in extensile fluids. (*SI Appendix*, Fig. S8). This is due to the correspondence between extensile flow aligning and contractile flow tumbling active liquid crystals (55).

Interface Self-Folding and Droplet Invagination

Polymer concentration controls the magnitude of the interfacial tension. So far, we studied "high" interfacial tension samples where PEG and dextran strongly separate. Decreasing polymer concentration reduced the surface tension, increased the magnitude of the interfacial deformations, and led to a qualitatively new behavior. When deformations increased above a critical threshold, the interface folded onto itself, invaginating passive droplets into the active phase (Fig. 6 and Movies S3 and S4). All such events followed a universal pathway: An initial valley-like interfacial deformation developed into a deep canyon-like structure that grew in depth over time. Eventually, the canyon walls merged, producing a passive droplet entirely enveloped by the active phase. Repeating invagination events created an active phase perforated by passive droplets (Fig. 7*A* and Movies S5–S7). Notably, the break-up of the continuous interface also exhibited a pronounced asymmetry. While we observed frequent invagination of passive droplets within the active phase, the reverse process where active dextran droplets were ejected into the passive phase was exceedingly rare if ever observed (Movie S6).

We analyzed the structure of the perforated active phase by measuring the position and size of the passive droplets and computing their total volume within the active phase as a function of time (Fig. 7*C*). The total volume was initially zero. It increased rapidly after $t = 1.2$ h, when the interface deformations were large enough to generate invaginations. This increase continued with time, with no hint of saturation over the sample lifetime. When compared to the "low" surface tension sample the droplet volume in the "higher" surface tension sample increased more slowly and remained smaller. Passive droplets have a lower density than the active fluid. Thus, they creamed toward the PEG/dextran interface creating a perforated foam-like region of the active fluid. Due to gravity mismatch, the density of the droplets varied with the vertical distance from the interface. The fraction of PEG droplets decayed exponentially with increasing distance from the interface (Fig. 8*B*).

Using the continuum model, we investigated how increasing activity influences interface behaviors. Beyond a critical value α_c, we observed the envelopment of passive droplets by a pathway similar to experiments (Fig. 6). To quantify the onset of droplet invagination, we computed the total area fraction of passive fluid that is enveloped by the active phase. For low activity, the total droplet volume is zero. Above α_c, the interface starts to fold onto itself and the total area of invaginated passive droplets becomes finite, increasing in time and quickly reaching a nonzero steady state value (*SI Appendix*, Fig. S10*B*). The steady state droplet area obtained from simulations increases monotonically with activity, saturating at the largest activity (Fig. 7*D*). In experiments the total volume of invaginated droplets increases as a function of time and does not saturate within the time scales of observation (Fig. 7*C*). We found a similar discrepancy in the magnitude of interfacial fluctuations, which saturates in simulations, but grows in time in experiments. These observations suggest a sort of aging of the experimental system, where the active stress increases with time. The microscopic mechanism for this is not understood.

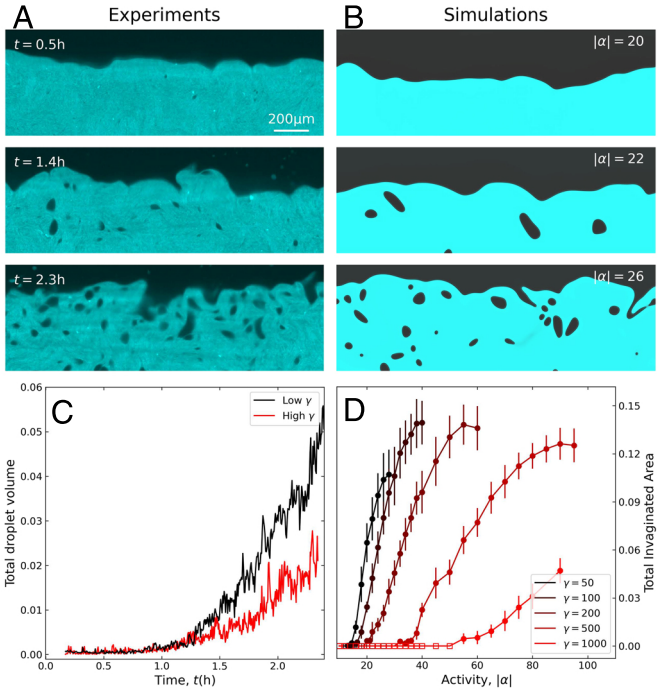

Fig. 7. Continuous interface breakage and droplet formation. (*A*) Conformation of a "low"-tension interface at different times. The sample had 183 nM KSA. (*B*) Dependence of an interface structure on activity. Surface tension is $\gamma = 200.0$. (*C*) The total volume of enveloped passive droplets as a function of time normalized by the volume of the active phase, for "low" and "high" surface tension samples. Once the fluctuation increased to a sufficiently large value at $t = 1.2$ h, the invagination events took place, and the volume of enveloped droplets increased linearly. (*D*) Mean total area of the passive droplets in the active phase in steady state (normalized by the total initial amount of active fluid) as a function of activity, for different values of surface tension.

We use the total droplet volume as an order parameter to quantify the transition to the perforated active state. The interfacial tension controls the location of the transition, with higher tension samples requiring higher activity (Fig. 7*D*). Intriguingly all the plots of droplet volume as a function of activity collapse onto a master curve by rescaling the activity (Fig. 9*A*). Using these data, we constructed a phase diagram showing the stability of bulk phase separation versus a perforated state as a function of activity and interfacial tension (Fig. 9*B*). For $|\alpha| < \alpha_c$ there are asymmetric interfacial fluctuations but no droplet formation. For $|\alpha| > \alpha_c$ the active fluid is perforated by passive droplets that are then continuously advected and sheared by the spontaneous flows. The critical activity α_c grows linearly with the interfacial tension: $\alpha_c = (\gamma + \gamma_0)/\ell$, where γ_0 and ℓ as fitting parameters independent of activity (*Inset* of Fig. 9*A*). The length scale ℓ depends on the nematic stiffness K and condensation energy r and seems to be of order of the nematic correlation length.

In the simulations, invaginated droplets can break apart or evaporate through diffusion (53). However, they are largely unable to overcome the elastic energy of the intervening liquid crystal and rarely merge with each other or with the bulk passive fluid (Movie S8). At moderate activities, this generates a steady state with a well-defined mean average droplet size (Fig. 9*C*). At larger activities, however, finite size effects become important as passive droplets are often advected to the bottom of the simulation box where they are replaced by active material due to boundary conditions $\phi(y = -L_y/2) = 1$ and $\phi(y = L_y/2) = 0$ (*Materials and Methods*). This, together with the constant release of interfacial curvature associated with droplet invagination, saturates the curvature asymmetry (Fig. 3*D*).

The transition to the perforated state correlates with the normalized asymmetry of the interfacial curvature $(\kappa_+ - \kappa_-)/\langle|\kappa|\rangle$, where $\langle|\kappa|\rangle = \int_{-\infty}^{\infty} d\kappa \rho(\kappa)|\kappa|$ is the mean of the magnitude of the local curvature. The transition to the perforated state occurs when the curvature asymmetry exceeds a threshold value, as is shown in Fig. 9*D*. A minimal condition for droplet invagination is that the active pressure $|\alpha|$ exceeds passive restoring pressure from surface tension and gravity $\sim \gamma/\ell + \Delta\rho g h$, where h and ℓ characterize the size of fluctuations. When these fluctuations grow large enough, passive droplets are enveloped by the active phase in the regions of high negative curvature (Fig. 6). When activity is increased above α_c, the mean curvature asymmetry decreases as more droplets are pinched off at the interface. The interface folding, however, is affected by surface tension, which controls the droplet shape and size. This is why the simple scaling ansatz fails for $|\alpha| > \alpha_c$.

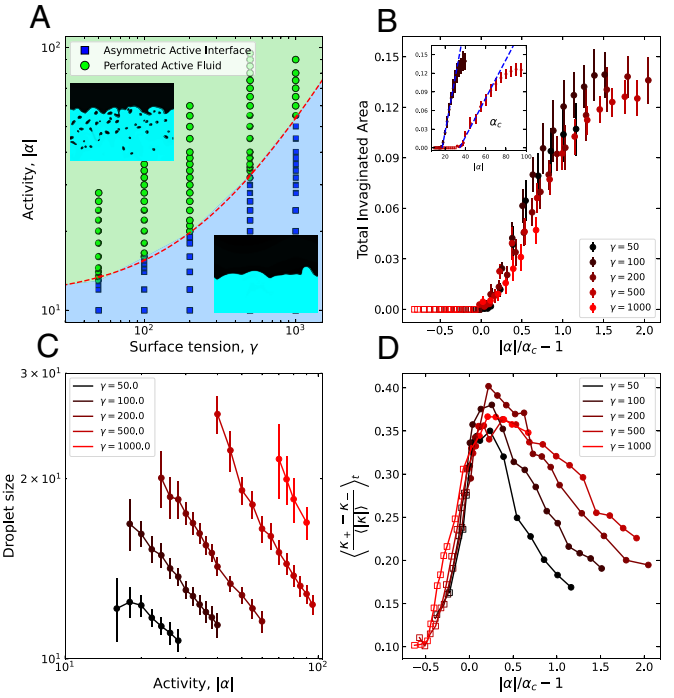

Fig. 9. Phase diagram of active interfaces. (*A*) The phase diagram in the activity/tension plane showing the transition from asymmetric interface fluctuations to interface folding. The critical activity α_C for the transition is identified numerically as described in the *Inset* of frame B. It is well fitted by $\alpha_C = (\gamma + \gamma_0)/\ell$ (red dashed line), where γ_0 and ℓ are fitting parameters. *Insets*: snapshots of the phase field ϕ at steady state in each phase (asymmetric interface: $\alpha = -18$, $\gamma = 200$; perforated state: $\alpha = -28$, $\gamma = 200$). (*B*) Total area fraction of passive fluid enveloped by the active fluid as a function of scaled activity $|\alpha|/\alpha_C - 1$ for various values of interface tension γ. *Inset*: the blue dashed lines are linear fits to the total droplet area fraction versus $|\alpha|$ plot (shown for $\gamma = 100, 500$). The intersection of each line with the zero area axis identifies the critical activity α_C. (*C*) The dependence of the droplet mean size on $|\alpha|$ for various interfacial tensions. (*D*) Normalized mean curvature asymmetry of the interface versus scaled activity $|\alpha|/\alpha_C - 1$ for various γ. The transition to the perforated phase with the onset of folding at α_C corresponds to a threshold value of this curvature asymmetry. At activities above α_C, the asymmetry decreases due to droplet folding in high-curvature regions of the interface.

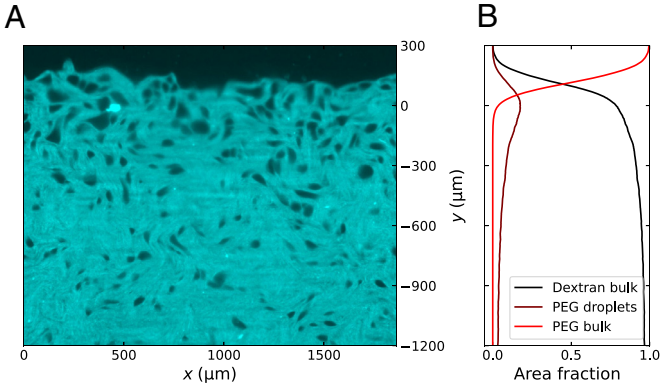

Fig. 8. The active fluid perforated with passive PEG droplets. (*A*) Two-dimensional cross-sections of the perforated active phase at $t = 2.9$ h. (*B*) Fractions of bulk dextran phase, PEG droplets, and bulk PEG phase at each depth y in the same frame. The gravitational field points along negative y. The sample contained 183 nM KSA, 2.0% PEG, and 2.0% dextran.

Discussion

We studied the behavior of bulk active interfaces. Our work revealed an up–down asymmetry of the interfacial fluctuations driven by an active fluid. We showed that such symmetry breaking is due to interface-adjacent vortical flows generated by active stresses located only on one interface side. At higher activities, we observed giant interfacial fluctuations, which led to the self-folding of the interface and the formation of passive droplets enveloped by the active fluid. These behaviors were observed in both experiments and numerical simulations. They should be common to all extensile active fluids with liquid crystalline degrees of freedom.

We compare our findings to previous work that studied active interfaces in quasi-2D samples confined between vertical glass walls separated by 60 μm spacers (35). Confined interfaces did not exhibit measurable asymmetries. This difference can be understood using our 2D model. In the confined samples, walls

screen the range of active flows (12). Incorporating this effect into the numerical model through frictional damping in the Stokes equation, as was done in ref. 35, yielded no measurable asymmetry of interfacial fluctuations. In contrast, the 2D model employed here only includes internal viscous dissipation and no extrinsic friction, thus allowing long-ranged hydrodynamic flows, which in turn yield strong asymmetries of the interface. The qualitative differences between the confined 2D experiments, where friction is important and the bulk 3D samples studied here, as well as between 2D simulations with and without friction highlight the key role of long-ranged active flows in generating asymmetric fluctuations of active interfaces. Importantly, other interfacial properties such as roughening exponents and the scaling of correlation length are known to strongly depend on dimensionality (56, 57). While our work successfully reproduces the main phenomenological properties of the 3D experimental system in a 2D simulation, a proper comparison of, for instance, roughening properties, requires computationally extensive three-dimensional simulations.

Experimentally we do not have a sufficient time resolution to track passive droplets enveloped by the active phase. Even without such data, however, we can make several qualitative observations. First, the lighter enveloped droplets accumulated near the active–passive interface. Once there they were persistently separated from the bulk passive fluid by a thin layer of active fluid (Movie S5). Thus passive droplets rarely merge back with the bulk passive fluid. We also rarely observed the merger of two droplets. The same behavior was found in numerical simulations. These observations suggest the presence of an effective repulsion between a pair of droplets or a droplet and the bulk interface.

In the high-activity regime, at late times the total volume of enveloped droplets increases linearly with time at a rate $\approx 1.7 \times 10^4 \mu m^3/s$ (Fig. 7*C*). Imaging data reveal roughly one invagination event per volume of $4 \times 10^4 \mu m^3$ for each frame taken every 4.3 s. This allows us to roughly estimate that the flux due to invagination is $\approx 1 \times 10^4 \mu m^3/s$, which is comparable to the rate of volume increase. This supports our claim that once invaginated, droplets remain trapped in the bulk active phase.

We hypothesize that repulsion between two passive droplets and passive droplet and bulk interface results from active anchoring, which creates an interface-bound aligned layer of the liquid crystals. When the interface is deformed, the resulting elastic energy maintains the separation between interfaces (Fig. 10). This elastic repulsion between interfaces separated by active fluid regions becomes important when the separation is comparable to the alignment length, which in turn is of the order of the active length. This effect could also stabilize the perforated active phase, preventing the merging of passive droplets back into the passive bulk fluid. This repulsive interaction may, however, be modified by active forces (58), which also contribute to controlling the nature of the alignment.

We elucidated two complementary mechanisms that lead to asymmetry of active interfaces over a broad range of activities. The interface breaks the symmetry of the fundamental bend instability, while nematic elasticity suppresses the merging of passive droplets and the break-up of bulk active phase into finite-sized droplets. These are, however, just partial ingredients required to develop a complete model of deformable active interfaces. For example, in a bulk fluid, the fully developed bend instability leads to local fracture and generation of topological defects (2). The interactions of topological defects with a soft interface is a fertile and relatively unexplored area. Defects deform soft interfaces asymmetrically. In turn, asymmetric interfaces can control the spatial nucleation of topological defects and their subsequent motility (*SI Appendix*, Fig. S7) (36, 40, 41, 59, 60).

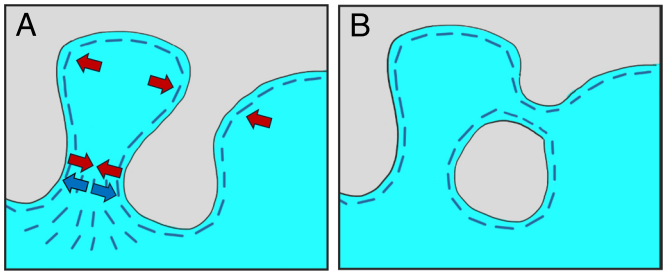

Fig. 10. Origin of the asymmetry of droplet splitting at the interface. The dashed line along the interface illustrates active anchoring which yields an aligned interfacial nematic layer. (*A*) Extensile active forces in the active fluid (red arrows) enhance any curvature of the interfacial nematic layer, promoting the splitting of droplets. At the neck of a protrusion, however, deformations are impeded by elastic forces arising from deformations of the aligned interfacial layer (blue arrows). This leads to an effective repulsion between two interfaces separated by a nematic region. Such repulsions become important when the thickness of the active neck is comparable to the alignment length. They prevent the release of active droplets into the passive phase. The same elastic repulsion prevents passive droplets, once invaginated, from merging back with the bulk passive fluid (Movie S9). (*B*) The invagination of a passive droplet into the active phase requires the lateral growth of the vertical walls and the reduction of the intervening passive region. The two vertical walls merge easily, as the intervening passive region can shrink without raising elastic energy, and hence does not impede this process.

We note a broad qualitative agreement between experiments and theory. There are, however, also differences. First, simulations reach a dynamical steady state, as evidenced by the total volume of enveloped droplets that saturate at long times (*SI Appendix*, Fig. S10). The experimental system, in contrast, shows no sign of reaching a steady state. One reason is that in theory, it is easy to fix activity. In comparison, several observations suggest that the activity in microtubule-based fluids increases over time (Figs. 3*B* and 7*C*). This complicates the mapping between activity, KSA concentration, and time and makes the dependence of asymmetry on activity very noisy. This aging effect could also be causing growth of the volume of the passive phase trapped in the active fluid (Fig. 7*C*). Another reason for this difference is that in simulations invaginated droplets split into smaller droplets which can then evaporate via an Ostwald ripening-like process. This process of Oswald-like ripening is not observed in experiments. Another notable difference is that in experiments, the mean size of individual invaginated passive droplets gets larger with time (*SI Appendix*, Fig. S15), while it decreases with increasing activity in simulations (Fig 9*C* and *SI Appendix*, S10). The distribution of curvatures obtained in simulations exhibits a small subexponential behavior for $\kappa > 0$ (Fig. 3*C*). This does not appear in the experimental distribution. We do not yet understand this discrepancy.

The perforated active phase qualitatively resembles the microphase-separated state predicted in a scalar model of active phase separation (61). There are, however, important differences. In the scalar model, active forces only act at the interface resulting in an effective negative interfacial tension. In our system, in contrast, liquid crystalline degrees of freedom and associated active flows in the bulk liquid crystal play an important role in driving the asymmetry of interfacial fluctuations and droplet invagination. Whether the interface between the active liquid crystal and a passive fluid can be described by a model using an effective single scalar model is an open question.

More broadly, we note intriguing yet poorly explored similarities between active phase separation and phase separation of two immiscible viscoelastic polymers (62). Upon phase separation of two polymers with very different relaxation times, one often observes the creation of a sponge-like network of the slow component trapped inside the fast phase, with an associated shrinking of the volume of the bulk slow phase (63). This phenomenon arises from the asymmetric distribution of viscoelastic stresses among the two components and it is a long-lived transient, with the long stages of viscoelastic phase separation approaching the behavior of conventional fluid phase separation, as described, for instance, by Model H (64). In the absence of activity, our system consists of two phase separating polymers, PEG and dextran, but their passive phase separation is not affected by viscoelasticity: The volumes of the two bulk phases remain constant during phase separation and no trapping of one phase into the other is observed. In the presence of activity, however, the two components have vastly different dynamics, as active stresses act directly only on the active dextran/MT liquid crystals and accelerate their dynamics relative to that of the passive PEG fluid. Additionally, the coupling of the interfacial dynamics which is driven by active flows, to the dynamics of the nematic texture introduces an "effective viscoelasticity" in the system due to the time lag between interface and texture relaxation. The perforated active phase bears qualitative similarities with the sponge-like state observed in viscoelastic phase separation but does not appear to be a transient state. Investigating the connections between active and viscoelastic phase separation is an interesting direction for future work.

Our findings have broad implications. For example, in biology, the stress-generating cytoskeleton interacts with membraneless organelles and lipid membranes, driving their nonequilibrium fluctuations and associated processes such as endo- and exocytosis. Our results have implications for understanding these complex interactions. From a material science perspective, a self-folding active interface provides a pathway for generating finite-sized droplets and vesicles, by a mechanism that is fundamentally different from the current microfluidic technologies.

Materials and Methods

Protein Purification. Tubulin monomers were purified and labeled by established protocols (65). 3% of tubulin was labeled with Alexa Fluor 647 NHS Ester (Invitrogen) using a Succinimidyl ester linker. The labeled and unlabeled tubulin were polymerized together into MT with 0.6 mM guanylyl-(alpha,beta)-methylene-diphosphonate (GMPCPP) (Gena Biosciences) and 1.2 mM Dithiothreitol (DTT) in M2B buffer(65). The M2B Buffer contained 1 mM ethylene glycol-bis(β-aminoethyl ether)-N,N,N′,N′-tetraacetic acid (EGTA), 2 mM MgCl2, and 80 mM piperazine-N,N′-bis(2-ethanesulfonic acid) (PIPES) in water and the pH was set to 7 (65). The final concentrations of MTs in the samples were 0.67 mg/mL. Kinesin-401 protein fused to a biotin-carboxyl carrier domain was expressed and purified by established protocols (65). It was then attached to tetrameric streptavidin in an M2B buffer with 5 mM DTT, forming a KSA. The final concentrations of KSA in the samples varied from 42 to 183 nM.

PEG-Dextran Active Phase Separation. The active phase separated samples were based on the previously published protocol, with several modifications (35). Previous experiments used a mixture of 35 kDa PEG and 2 MDa dextran. Activity in these samples could only be sustained by a specific polymer concentration, which did not allow for the control of the surface tension. Therefore, we changed the protocol for the phase separation. We added PEG (100 kDa, Sigma-Aldrich) and dextran (450 to 650 kDa, Sigma-Aldrich) into M2B buffer (80 mM K-pipes, 2 mM $MgCl_2$, 1 mM EGTA, pH 6.8). For visualization, we added a small amount of amino-dextran [Fina Biosolutions, (<0.1% w/w final concentration)] labeled with Alexa-Fluor 488 NHS Ester (Invitrogen). The final sample contained 2.0 to 2.1% (w/w) PEG and 2.0 to 2.1% (w/w) dextran.

The MTs and KSA were added to the PEG-dextran mixture with ATP (3 mM final), antioxidants, and an ATP regeneration system made by established protocols (35). The antioxidants contained (in final concentrations) 2 mM Trolox, 5 mM DTT, 3.3 mg/mL glucose, 200 μg/mL glucose oxidase, and 35 μg/mL catalase dissolved in a phosphate buffer (20 mM K_2HPO_4 and 100 mM KCl in deionized water, pH 7.4). The ATP regeneration system contained (in final concentrations) 26 mM phosphoenol Pyruvate (Beantown Chemical) and pyruvate kinase/lactate dehydrogenase (Sigma Aldrich) dissolved in M2B.

Chamber. The sample was contained in a transparent fluorinated ethylene propylene (FEP) tube with an inner diameter of 2.4 mm, outer diameter of 4.0 mm, and refractive index of 1.344. The FEP tube was placed into a slightly larger aluminum tube and heated in an oven with 80 °C for 20 min for straightening (66). The tube was sonicated (Branson 3800) in 1 M potassium hydroxide for 30 min and 190 proof ethanol for 30 min and stored in 10% (w/w) Pluronic F-127 (Sigma-Aldrich) solution in water. The tube was sealed from the bottom with UV glue and parafilm. It was mounted to the microscope from the top.

Microscopy. The sample was loaded into the FEP tube with a pipette and centrifuged at 2,000 g relative centrifugal force for 1 min (Fisher Scientific, 05-090-128) to bulk separate the PEG-rich and dextran-rich phases. The tube was mounted onto a laser sheet microscope (Zeiss Z.1 Lightsheet) and imaged for 3 h. The tube was immersed in water contained in a cubic transparent container to keep the optical path the same during 3D acquisition. The temperature was 20 °C. The illumination objectives (5× 0.1 NA) create the laser sheet from both sides of the samples. The imaging objective was 5× 0.16 NA. The illumination lasers were 488 nm for the dextran channel and 638 nm for MT channel. In each time frame, $x-y$ images with step size $\Delta z = 20\mu$m were taken from the center of the tube, generating a 3D image stack.

3D Curvature. To quantify the interface, we extracted the boundary between the two phases from the dextran-channel image, which uses a machine-learning algorithm to classify the image based on intensity thresholding (67). The 3D interface was transformed into a mesh form using the software MeshLab (68). The mean curvature on the interface was defined as the average of the 2D curvatures in the $x-y$ and $y-z$ plane and calculated using discrete exterior calculus (69, 70).

Numerical Simulations. The equations for the continuum model (Eq. **1**) were solved using self-developed pseudospectral solvers (71, 72). The equations were solved on a two-dimensional grid of size 1,024 × 1,024, with grid spacing fixed to be $\Delta x = \Delta y = \sqrt{2/3}$, small enough to accurately resolve the interface between the active and passive phases (which is the smallest length scale in the system). Time evolution consisted of a simple backward Euler time stepping, with $\Delta t \in [10^{-5}, 10^{-4}]$, simulated for a total of 10^6 to 10^7 time steps. We consider periodic boundaries in the horizontal (x) direction, and in the vertical direction (y), we consider no-slip boundaries, with $\phi = 0, 1$ fixed at the top and bottom boundaries respectively, consistent with the gravitational force (i.e heavier active phase on the bottom). The system is initialized to be bulk phase separated, with equal volumes of the active and the passive phases and the active phase at the bottom, $\phi(x, y, t = 0) = \Theta(-y)$. Refer to *SI Appendix* for additional details.

Data, Materials, and Software Availability. Experimental data of all interface curvatures and droplet invagination, images, and corresponding analysis codes have been deposited in Dryad (DOI: 10.5061/dryad.b8gtht7n0) (72). Simulation code is available at https://github.com/paarthgulati/activeFolding_cuPSS (73). All other data are included in the article and/or supporting information.

ACKNOWLEDGMENTS. This work was primarily supported by the US Department of Energy, Office of Basic Energy Sciences under award number DE-SC0019733. Development and optimization of the two-phase system of active liquid–liquid phase separation was supported by NSF-ISS-2224350. We also acknowledge the use of the biosynthesis facility supported by NSF-MRSEC-2011846 and NRI-MCDB Microscopy Facility supported by the NIH Shared Instrumentation Grant 1S10OD019969-01A1. Use was made of computational facilities purchased with funds from the NSF (CNS-1725797) and administered by the Center for Scientific Computing (CSC). The CSC is supported by the California NanoSystems Institute and the Materials Research Science and Engineering Center (NSF DMR 2308708).

Author affiliations: [a]Department of Physics, University of California, Santa Barbara, CA 93106; [b]Department of Physics, Brandeis University, Waltham, MA 02453; [c]School of Physics, College of Sciences, Georgia Institute of Technology, Atlanta, GA 30332; [d]Department of Molecular Biophysics and Biochemistry, Yale University, New Haven, CT 06520; and [e]Interdisciplinary Program in Quantitative Biosciences, University of California, Santa Barbara, CA 93106

1. R. Aditi Simha, S. Ramaswamy, Hydrodynamic fluctuations and instabilities in ordered suspensions of self-propelled particles. *Phys. Rev. Lett.* **89**, 058101 (2002).
2. T. Sanchez, D. T. N. Chen, S. J. DeCamp, M. Heymann, Z. Dogic, Spontaneous motion in hierarchically assembled active matter. *Nature* **491**, 431–434 (2012).
3. L. Giomi, M. J. Bowick, P. Mishra, R. Sknepnek, M. Cristina Marchetti, Defect dynamics in active nematics. *Philos. Trans. R. Soc. A Math. Phys. Eng. Sci.* **372**, 20130365 (2014).
4. S. Zhou, A. Sokolov, O. D. Lavrentovich, I. S. Aranson, Living liquid crystals. *Biophys. J.* **106**, 420a (2014).
5. S. P. Thampi, R. Golestanian, J. M. Yeomans, Instabilities and topological defects in active nematics. *Europhys. Lett.* **105**, 18001 (2014).
6. L. Giomi, Geometry and topology of turbulence in active nematics. *Phys. Rev. X* **5**, 031003 (2015).
7. T. Gao, R. Blackwell, M. A. Glaser, M. D. Betterton, M. J. Shelley, Multiscale polar theory of microtubule and motor-protein assemblies. *Phys. Rev. Lett.* **114**, 048101 (2015).
8. P. Guillamat, J. Ignés-Mullol, F. Sagués, Control of active liquid crystals with a magnetic field. *Proc. Natl. Acad. Sci. U.S.A.* **113**, 5498–5502 (2016).
9. B. Martínez-Prat, J. Ignés-Mullol, J. Casademunt, F. Sagués, Selection mechanism at the onset of active turbulence. *Nat. Phys.* **15**, 362–366 (2019).
10. R. Alert, J. F. Joanny, J. Casademunt, Universal scaling of active nematic turbulence. *Nat. Phys.* **16**, 682–688 (2020).
11. N. Kumar, R. Zhang, J. J. De Pablo, M. L. Gardel, Tunable structure and dynamics of active liquid crystals. *Sci. Adv.* **4**, eaat7779 (2018).
12. P. Chandrakar *et al*., Confinement controls the bend instability of three-dimensional active liquid crystals. *Phys. Rev. Lett.* **125**, 257801 (2020).
13. A. Sokolov, A. Mozaffari, R. Zhang, J. J. de Pablo, A. Snezhko, Emergence of radial tree of bend stripes in active nematics. *Phys. Rev. X* **9**, 031014 (2019).
14. L. C. Head *et al*., Spontaneous self-constraint in active nematic flows. *Nat. Phys.* **20**, 492–500 (2024).
15. H. Wioland, F. G. Woodhouse, J. Dunkel, J. O. Kessler, R. E. Goldstein, Confinement stabilizes a bacterial suspension into a spiral vortex. *Phys. Rev. Lett.* **110**, 268102 (2013).
16. D. Nishiguchi, I. S. Aranson, A. Snezhko, A. Sokolov, Engineering bacterial vortex lattice via direct laser lithography. *Nat. Commun.* **9**, 4486 (2018).
17. K. T. Wu *et al*., Transition from turbulent to coherent flows in confined three-dimensional active fluids. *Science* **355**, eaal1979 (2017).
18. A. Opathalage *et al*., Self-organized dynamics and the transition to turbulence of confined active nematics. *Proc. Natl. Acad. Sci. U.S.A.* **116**, 4788–4797 (2019).
19. M. Theillard, R. Alonso-Matilla, D. Saintillan, Geometric control of active collective motion. *Soft Matter* **13**, 363–375 (2017).
20. T. N. Shendruk, A. Doostmohammadi, K. Thijssen, J. M. Yeomans, Dancing disclinations in confined active nematics. *Soft Matter* **13**, 3853–3862 (2017).
21. M. Varghese, A. Baskaran, M. F. Hagan, A. Baskaran, Confinement-induced self-pumping in 3D active fluids. *Phys. Rev. Lett.* **125**, 268003 (2020).
22. S. Chandragiri, A. Doostmohammadi, J. M. Yeomans, S. P. Thampi, Flow states and transitions of an active nematic in a three-dimensional channel. *Phys. Rev. Lett.* **125**, 148002 (2020).
23. P. Gulati, S. Shankar, M. C. Marchetti, Boundaries control active channel flows. *Front. Phys.* **10**, 948415 (2022).
24. J. Y. Tinevez *et al*., Role of cortical tension in bleb growth. *Proc. Natl. Acad. Sci. U.S.A.* **106**, 18581–18586 (2009).
25. J. Sedzinski *et al*., Polar actomyosin contractility destabilizes the position of the cytokinetic furrow. *Nature* **476**, 462–466 (2011).
26. G. Salbreux, J. Prost, J. F. Joanny, Hydrodynamics of cellular cortical flows and the formation of contractile rings. *Phys. Rev. Lett.* **103**, 058102 (2009).
27. A. C. Reymann, F. Staniscia, A. Erzberger, G. Salbreux, S. W. Grill, Cortical flow aligns actin filaments to form a furrow. *eLife* **5**, e17807 (2016).
28. J. F. Joanny, S. Ramaswamy, A drop of active matter. *J. Fluid Mech.* **705**, 46–57 (2012).
29. E. Tjhung, D. Marenduzzo, M. E. Cates, Spontaneous symmetry breaking in active droplets provides a generic route to motility. *Proc. Natl. Acad. Sci. U.S.A.* **109**, 12381–12386 (2012).
30. M. L. Blow, S. P. Thampi, J. M. Yeomans, Biphasic, lyotropic, active nematics. *Phys. Rev. Lett.* **113**, 248303 (2014).
31. L. Giomi, A. DeSimone, Spontaneous division and motility in active nematic droplets. *Phys. Rev. Lett.* **112**, 147802 (2014).
32. M. Paoluzzi, R. Di Leonardo, M. C. Marchetti, L. Angelani, Shape and displacement fluctuations in soft vesicles filled by active particles. *Sci. Rep.* **6**, 1–10 (2016).
33. C. J. Miles, A. A. Evans, M. J. Shelley, S. E. Spagnolie, Active matter invasion of a viscous fluid: Unstable sheets and a no-flow theorem. *Phys. Rev. Lett.* **122**, 098002 (2019).
34. H. Soni, W. Luo, R. A. Pelcovits, T. R. Powers, Stability of the interface of an isotropic active fluid. *Soft Matter* **15**, 6318–6330 (2019).
35. R. Adkins *et al*., Dynamics of active liquid interfaces. *Science* **377**, 768–772 (2022).
36. Y. N. Young, M. Shelley, D. Stein, The many behaviors of deformable active droplets. *Math. Biosci. Eng.* **18**, 2849–2881 (2021).
37. F. Kempf, R. Mueller, E. Frey, J. M. Yeomans, A. Doostmohammadi, Active matter invasion. *Soft Matter* **15**, 7538–7546 (2019).
38. R. Alert, Fingering instability of active nematic droplets. *J. Phys. A Math. Theor.* **55**, 234009 (2022).
39. R. C. Coelho, N. A. Araújo, M. M. T. da Gama, Propagation of active nematic-isotropic interfaces on substrates. *Soft Matter* **16**, 4256–4266 (2020).
40. H. Xu, M. R. Nejad, J. M. Yeomans, Y. Wu, Geometrical control of interface patterning underlies active matter invasion. *Proc. Natl. Acad. Sci. U.S.A.* **120**, e2219708120 (2023).
41. L. J. Ruske, J. M. Yeomans, Morphology of active deformable 3D droplets. *Phys. Rev. X* **11**, 021001 (2021).
42. F. C. Keber *et al*., Topology and dynamics of active nematic vesicles. *Science* **345**, 1135–1139 (2014).
43. S. C. Takatori, A. Sahu, Active contact forces drive nonequilibrium fluctuations in membrane vesicles. *Phys. Rev. Lett.* **124**, 158102 (2020).
44. H. R. Vutukuri *et al*., Active particles induce large shape deformations in giant lipid vesicles. *Nature* **586**, 52–56 (2020).
45. I. Vélez-Cerón, P. Guillamat, F. Sagués, J. Ignés-Mullol, Probing active nematics with in situ microfabricated elastic inclusions. *Proc. Natl. Acad. Sci. U.S.A.* **121**, e2312494121 (2024).
46. G. Kokot, H. A. Faizi, G. E. Pradillo, A. Snezhko, P. M. Vlahovska, Spontaneous self-propulsion and nonequilibrium shape fluctuations of a droplet enclosing active particles. *Commun. Phys.* **5**, 91 (2022).
47. A. M. Tayar *et al*., Controlling liquid-liquid phase behaviour with an active fluid. *Nat. Mater.* **22**, 1401–1408 (2023).
48. A. Sciortino *et al*., Active membrane deformations of a minimal synthetic cell. bioRxiv [Preprint] (2023). https://doi.org/10.1101/2023.12.18.571643 (Accessed 12 November 2024).
49. Y. Liu, R. Lipowsky, R. Dimova, Concentration dependence of the interfacial tension for aqueous two-phase polymer solutions of dextran and polyethylene glycol. *Langmuir* **28**, 3831–3839, PMID: 22292882 (2012).
50. F. Hilitski *et al*., Measuring cohesion between macromolecular filaments one pair at a time: Depletion-induced microtubule bundling. *Phys. Rev. Lett.* **114**, 138102 (2015).
51. P. Srivastava, P. Mishra, M. C. Marchetti, Negative stiffness and modulated states in active nematics. *Soft Matter* **12**, 8214–8225 (2016).
52. S. Santhosh, M. R. Nejad, A. Doostmohammadi, J. M. Yeomans, S. P. Thampi, Activity induced nematic order in isotropic liquid crystals. *J. Stat. Phys.* **180**, 699–709 (2020).
53. F. Caballero, M. C. Marchetti, Activity-suppressed phase separation. *Phys. Rev. Lett.* **129**, 268002 (2022).
54. R. C. Coelho, H. R. Figueiredo, M. M. T. da Gama, Active nematics on flat surfaces: From droplet motility and scission to active wetting. *Phys. Rev. Res.* **5**, 033165 (2023).
55. L. Giomi, T. B. Liverpool, M. C. Marchetti, Sheared active fluids: Thickening, thinning, and vanishing viscosity. *Phys. Rev. E* **81**, 051908 (2010).
56. M. Kardar, G. Parisi, Y. C. Zhang, Dynamic scaling of growing interfaces. *Phys. Rev. Lett.* **56**, 889 (1986).
57. F. Caballero, A. Maitra, C. Nardini, Interface dynamics of wet active systems. arXiv [Preprint] (2024). https://arxiv.org/abs/2409.02288 (Accessed 12 November 2024).
58. L. Neville, J. Eggers, T. Liverpool, Controlling wall -particle interactions with activity. *Soft Matter* **20**, 8395–8406 (2024).
59. K. Chaithanya *et al*., Transport of topological defects in a biphasic mixture of active and passive nematic fluids. *Commun. Phys.* **7**, 2399–3650 (2024)
60. S. Bhattacharyya, J. M. Yeomans, Phase ordering in binary mixtures of active nematic fluids. *Phys. Rev. E* **110**, 024607 (2024).
61. G. Fausti, E. Tjhung, M. Cates, C. Nardini, Capillary interfacial tension in active phase separation. *Phys. Rev. Lett.* **127**, 068001 (2021).
62. H. Tanaka, Viscoelastic phase separation. *J. Phys. Condens. Matter* **12**, R207 (2000).
63. H. Tanaka, Universality of viscoelastic phase separation in dynamically asymmetric fluid mixtures. *Phys. Rev. Lett.* **76**, 787 (1996).
64. P. M. Chaikin, T. C. Lubensky, T. A. Witten, *Principles of Condensed Matter Physics* (Cambridge University Press Cambridge, 1995), vol. 10.
65. A. M. Tayar, L. M. Lemma, Z. Dogic, *Assembling Microtubule-Based Active Matter*, H. Inaba, Ed. (Springer US, New York, NY, 2022), pp. 151–183.
66. A. Kaufmann, M. Mickoleit, M. Weber, J. Huisken, Multilayer mounting enables long-term imaging of zebrafish development in a light sheet microscope. *Development* **139**, 3242–3247 (2012).
67. S. Berg *et al*., ilastik: Interactive machine learning for (bio)image analysis. *Nat. Methods* **16**, 1226–1232 (2019).
68. P. Cignoni *et al*., "MeshLab: An open-source mesh processing tool" in *Eurographics Italian Chapter Conference*, V. Scarano, R. D. Chiara, U. Erra, Eds. (The Eurographics Association, 2008).
69. M. D. Keenan Crane, F. de Goes, P. Schröder, "Digital geometry processing with discrete exterior calculus" in *ACM SIGGRAPH 2013 courses, SIGGRAPH '13* (Association for Computing Machinery, New York, NY, 2013).
70. D. Cislo, N. P. Mitchell, Declab. GitHub repository. https://github.com/DillonCislo/DECLab. Accessed 12 November 2024.
71. F. Caballero, cuPSS: a package for pseudo-spectral integration of stochastic PDEs. arXiv [Preprint] (2024). https://arxiv.org/abs/2405.02410 (Accessed 12 November 2024).
72. L. Zhao, Asymmetric fluctuations and self-folding of active interfaces. Dryad (2024). https://doi.org/10.5061/dryad.b8gtht7n0. Deposited 12 November 2024.
73. Gulati, activeFolding_cuPSS. GitHub repository. https://github.com/paarthgulati/activeFolding_cuPSS. Accessed 12 November 2024.